Deep-Sea Research Part I xxx (xxxx) xxx–xxx

Contents lists available at ScienceDirect

Deep-Sea Research Part I

journal homepage: www.elsevier.com/locate/dsri

Natural spatial variability of depositional conditions, biogeochemical processes and element fluxes in sediments of the eastern Clarion-Clipperton Zone, Pacific Ocean

Jessica B. Volz[a,*], José M. Mogollón[b,c,d], Walter Geibert[a], Pedro Martínez Arbizu[e], Andrea Koschinsky[f], Sabine Kasten[a,g]

[a] Alfred Wegener Institute Helmholtz Centre for Polar and Marine Research, Bremerhaven, Germany
[b] Department of Marine Organic Biogeochemistry, NIOZ Royal Netherlands Institute for Sea Research, P.O. Box 59, Den Burg, the Netherlands
[c] Department of Earth Sciences – Geochemistry, Utrecht University, P.O. Box 80.021, 3508TA Utrecht, the Netherlands
[d] Institute of Environmental Sciences (CML), Leiden University, Einsteinweg 2, 2333CC Leiden, the Netherlands
[e] Senckenberg am Meer, DZMB, Wilhelmshaven, Germany
[f] Jacobs University Bremen, Department of Physics and Earth Sciences, Bremen, Germany
[g] University of Bremen, Faculty of Geosciences, Klagenfurter Strasse, Bremen, Germany

ARTICLE INFO

Keywords:
Deep-sea sediments
Redox zonation
Biogeochemical processes
Oxygen penetration depth
Eastern equatorial Pacific
CCZ
Manganese nodule belt

ABSTRACT

The manganese nodule belt within the Clarion and Clipperton Fracture Zones (CCZ) in the abyssal NE Pacific Ocean is characterized by numerous seamounts, low organic matter (OM) depositional fluxes and meter-scale oxygen penetration depths (OPD) into the sediment. The region hosts contract areas for the exploration of polymetallic nodules and Areas of Particular Environmental Interest (APEI) as protected areas. In order to assess the impact of potential mining on these deep-sea sediments and ecosystems, a thorough determination of the natural spatial variability of depositional and geochemical conditions as well as biogeochemical processes and element fluxes in the different exploration areas is required.

Here, we present a comparative study on (1) sedimentation rates and bioturbation depths, (2) redox zonation of the sediments and element fluxes as well as (3) rates and pathways of biogeochemical reactions at six sites in the eastern CCZ. The sites are located in four European contract areas and in the APEI3. Our results demonstrate that the natural spatial variability of depositional and (bio)geochemical conditions in this deep-sea sedimentary environment is much larger than previously thought. We found that the OPD varies between 1 and 4.5 m, while the sediments at two sites are oxic throughout the sampled interval (7.5 m depth). Below the OPD, manganese and nitrate reduction occur concurrently in the suboxic zone with pore-water Mn^{2+} concentrations of up to 25 μM. The thickness of the suboxic zone extends over depth intervals of less than 3 m to more than 8 m. Our data and the applied transport-reaction model suggest that the extension of the oxic and suboxic zones is ultimately determined by the (1) low flux of particulate organic carbon (POC) of 1–2 mg C_{org} m^{-2} d^{-1} to the seafloor, (2) low sedimentation rates between 0.2 and 1.15 cm kyr^{-1} and (3) oxidation of pore-water Mn^{2+} at depth. The diagenetic model reveals that aerobic respiration is the main biogeochemical process driving OM degradation. Due to very low POC fluxes of 1 mg C_{org} m^{-2} d^{-1} to the seafloor at the site investigated in the protected APEI3 area, respiration rates are twofold lower than at the other study sites. Thus, the APEI3 site does not represent the (bio)geochemical conditions that prevail in the other investigated sites located in the European contract areas. Lateral variations in surface water productivity are generally reflected in the POC fluxes to the seafloor across the various areas but deviate from this trend at two of the study sites. We suggest that the observed spatial variations in depositional and (bio)geochemical conditions result from differences in the degree of degradation of OM in the water column and heterogeneous sedimentation patterns caused by the interaction of bottom water currents with seafloor topography.

* Corresponding author.
E-mail address: jessica.volz@awi.de (J.B. Volz).

https://doi.org/10.1016/j.dsr.2018.08.006
Received 31 December 2017; Received in revised form 23 June 2018; Accepted 11 August 2018

1. Introduction

Vast deep-sea regions of the open Pacific Ocean are characterized by low fluxes of organic carbon to the seafloor (Lutz et al., 2007). The discovery of high abundances of polymetallic nodules in these carbon-starved environments in the equatorial Pacific Ocean during the *HMS Challenger* expedition (Murray and Renard, 1891) has driven the global economic interest in deep-sea mining (Mero, 1965) and has triggered several comprehensive studies in the area of the Clarion-Clipperton Zone (CCZ) (e.g., Chun, 1908; Bischoff and Piper, 1979; Bender, 1983; von Stackelberg and Beiersdorf, 1987; Lodge et al., 2014). Most geochemical studies on CCZ sediments have focused on polymetallic manganese nodules, more precisely their chemical and mineralogical composition as well as pathways of formation (e.g., Calvert and Price, 1977; Jeong et al., 1994; Wegorzewski and Kuhn, 2014). Only a few studies that combine pore-water and sediment geochemistry have been performed on sediments of the CCZ (e.g., Bischoff and Piper, 1979; Jahnke et al., 1982; Müller et al., 1988; Mewes et al., 2014; Mogollón et al., 2016). The upper few centimeters of the sediments in the CCZ are generally characterized by organic carbon (OC) contents of < 0.5 wt% (e.g., Arrhenius, 1952; Heath et al., 1977; Khripounoff et al., 2006). Below 30 cm, a residual OC fraction of ~ 0.1 wt% remains in the deeply buried sediments (Müller and Mangini, 1980; Müller et al., 1988; Mewes et al., 2014; Mogollón et al., 2016). Müller and Mangini (1980) have reported a sedimentation rate of 0.15–0.4 cm kyr^{-1} for the western CCZ. Slightly higher rates between 0.35 and 0.6 cm kyr^{-1} were determined by Mewes et al. (2014) for the eastern CCZ. In the framework of the MANOP (Manganese Nodule Project) study, sediments and associated pore water underlying the Pacific equatorial upwelling area between 0° and 10°N were analyzed (e.g., Emerson et al., 1980; Klinkhammer, 1980). The relatively high POC flux to the seafloor in this area (Lutz et al., 2007) causes a compressed redox zonation in the sediments with the occurrence of Mn^{2+} in the absence of oxygen and sulfide in the pore water after nitrate is consumed below 10 cm (Emerson et al., 1980; Klinkhammer, 1980; Jahnke et al., 1982). The study by Røy et al. (2012) was performed along a sampling transect at 0°N in the eastern Pacific Ocean and shows that the oxygen penetration depth (OPD) is generally 10 cm. Oxygen depletion in combination with the absence of sulfate reduction allows manganese reduction to extend over sediment intervals of up to 100 m (D'Hondt et al., 2004). Studies performed by Mewes et al. (2014) and Mogollón et al. (2016) in the German contract area "East" for the exploration of polymetallic nodules show that oxygen typically penetrates 1.8–3 m into the sediments between 11°–12°N and 117°–120°W. Below the oxic zone, manganese and nitrate reduction occur concurrently over depth intervals between 6 m to more than 12 m depth. In contrast, sediments underlying the carbon-starved waters of the North Pacific Gyre (NPG) are deeply oxygenated at least 30 m below the seafloor due to low respiration rates (Røy et al., 2012).

Considering that abyssal benthic communities are limited by low carbon export from the euphotic zone (e.g., Smith et al., 2008), biodiversity in the CCZ is surprisingly high (e.g., Glover et al., 2002). Vanreusel et al. (2016) have recently performed a comparative study of benthic faunal composition and densities in five areas in the CCZ over a distance of approximately 1300 km. This biological study revealed (1) lowest densities of both sessile and mobile fauna in the area with lowest POC fluxes to the seafloor, (2) a strong dependency of local biodiversity on manganese nodule abundance and (3) a reduction of the mobile fauna by at least 50% in areas where controlled anthropogenic disturbances were created 37 and 20 years ago. As these simulated deep-sea mining experiments cause the removal or alteration of top sediment layers, and the formation of large sediment plumes in the water column, the recovery of benthic communities after anthropogenic impacts is expected to be very slow (e.g., Miljutin et al., 2011; Jones et al., 2017; Boetius and Haeckel, 2018).

Due to the economic interest in the exploitation of deep-sea manganese nodules, the International Seabed Authority (ISA) has adopted an Environmental Management Plan (EMP) for the CCZ, which includes temporal contracts for the exploration of manganese nodules (ISA, 2010; Lodge et al., 2014; Madureira et al., 2016). In addition to this, nine areas have been designated for the conservation of natural resources, which are excluded from any mining activities and declared as "Areas of Particular Environmental Interest" (APEI). For the further development of an efficient EMP, Lodge et al. (2014) emphasize the necessity of environmental baseline studies including the determination of chemical parameters before and after anthropogenic disturbances.

In order to assess the natural spatial variability of geochemical conditions, biogeochemical processes, and element fluxes in the CCZ as needed for such baseline studies, we present a comparative study on (1) sedimentation rates and bioturbation depths, (2) redox zonation of sediments and oxygen fluxes, and (3) rates and pathways of biogeochemical reactions driving the degradation of organic matter in these deep-sea deposits. We have studied sediments of four European contract areas including the German BGR area "East" (Bundesanstalt für Geowissenschaften und Rohstoffe), the area of the eastern European consortium IOM (InterOceanMetal), the Belgian GSR area (Global Sea Mineral Resources NV), the French IFREMER area (Institut Français de Recherche pour l'Exploitation de la Mer) and one of the nine APEIs which is located north of the CCZ and referred to as the APEI3. Our work includes *ex situ* oxygen measurements, comprehensive pore-water and solid-phase analyses on the upper 10 m of sediment and the application of a one-dimensional steady-state reaction transport model.

2. Geological and oceanographic setting

The CCZ comprises an area of about 6 million km^2 in the equatorial Pacific Ocean defined by two major transform faults, the Clarion Fracture Zone in the north and the Clipperton Fracture Zone in the south (Halbach et al., 1988). The fracture zones are formed at the East Pacific Rise, stretch perpendicular to the spreading center, and enclose a vast seafloor covered by numerous seamounts and NNE-SSW oriented horst and graben structures (Johnson, 1972; ISA, 2010). The abyssal deep-sea pelagic sediments at 4–5 km water depth between 116°–155°W and 5°–15°N are dominated by biogenic sediments, notably siliceous oozes (Berger, 1974). The CCZ sedimentary records commonly have hiatuses caused by (1) erosion and redeposition of sediment elsewhere or (2) nondeposition (Johnson, 1972; Craig, 1979; von Stackelberg and Beiersdorf, 1991; Mewes et al., 2014). Average deep-water flow velocities of < 10 cm s^{-1} refute significant contemporary erosion, but distinct hiatuses in the Eocence to Quaternary sediments may have resulted from relatively higher current velocities (Craig, 1979; Theyer et al., 1985; von Stackelberg and Beiersdorf, 1987).

Average particulate organic carbon (POC) fluxes to the seafloor in the eastern CCZ are 1.5–1.8 mg C_{org} m^{-2} d^{-1} between 10° and 15°N and decline to 1.3 mg C_{org} m^{-2} d^{-1} north of 15°N (Lutz et al., 2007; Fig. 1a). As a consequence of microbial respiration in the water column and weak ocean ventilation, a pronounced oxygen minimum zone (OMZ) persists in the eastern equatorial Pacific (e.g., Wishner et al., 1995; Kalvelage et al., 2015). Oxygen measurements throughout the water column in the CCZ show a well-oxygenated upper mixed layer with a sharp oxycline particularly in the BGR and IOM areas (Martínez Arbizu and Haeckel, 2015). Below the oxycline, the OMZ extends over 100–1000 m and 100–800 m, respectively, with concentrations below 3 μM. The GSR and IFREMER areas show similar extents of the OMZ, however, lowest oxygen concentrations range between 3 and 16 μM. In the APEI3, the OMZ is located at 300–900 m water depth with minimum oxygen concentrations of 6–16 μM (Martínez Arbizu and Haeckel, 2015).

3. Material and methods

As part of the BMBF-EU JPI Oceans pilot action "Ecological Aspects

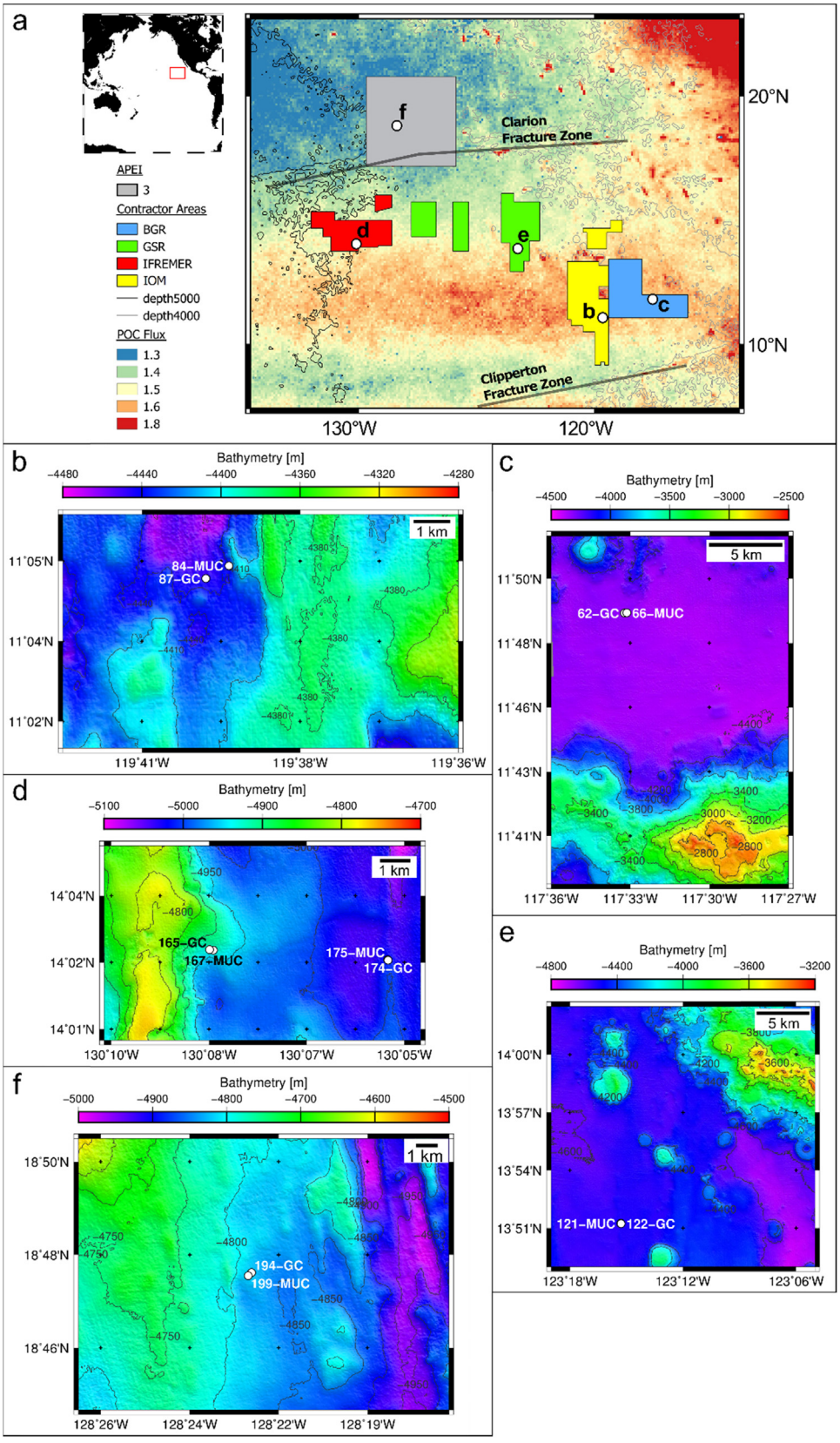

Fig. 1. Maps of the study area during RV SONNE cruise SO239 showing (a) the four investigated exploration areas in the CCZ, the APEI3 and the sampling stations (white circles). The background colors indicate the estimated upper limit in POC flux [mg C_{org} m^{-2} d^{-1}] to the seafloor by Lutz et al. (2007) (modified after Vanreusel et al., 2016). Detailed hydroacoustic maps created with the multibeam system EM122 (Martínez Arbizu and Haeckel, 2015; Greinert, 2016) show the locations of the sampling stations with b: IOM; c: BGR; d: IFREMER; e: GSR; f: APEI3. The maps were produced with GMT5 (Wessel et al., 2013). (For interpretation of the references to color in this figure legend, the reader is referred to the web version of this article.)

of Deep-Sea Mining (MiningImpact)" sediment cores were taken at five sites in the CCZ during RV SONNE cruise SO239 in March/April 2015 (Fig. 1; Martínez Arbizu and Haeckel, 2015). For the recovery of sediment cores, two different sampling devices were deployed in all investigated areas. A multiple corer (MUC) equipped with twelve 60 cm long tubes with an inner diameter of 9.4 cm was used for the retrieval of undisturbed surface sediments. For the recovery of long sediment cores of up to 10 m length a gravity corer (GC) with a 12 cm wide plastic liner was deployed (Table 1).

Table 1
MUC and GC cores investigated in this study including information on geographic position, water depth and core length. Nodule coverage shows the density and size of nodules recovered from the sediment surface at the box corer (BC) station nearest to MUC and GC locations. Nodule sampling area is 0.25 m^2, the length of scale (▬) corresponds to 10 cm.

Area	Station SO239-	Device	Latitude [N]	Longitude [W]	Water depth [m]	Core length [cm]	Nodule coverage
BGR	60	BC	11°48.46′	117°33.02′	4324.5		
BGR	62	GC	11°49.12′	117°33.22′	4312.2	900	
BGR	66	MUC	11°49.13′	117°33.13′	4314.8	36	
IOM	84	MUC	11°4.73′	119°39.48′	4430.8	43	
IOM	87	GC	11°4.54′	119°39.83′	4436	930	
IOM	89	BC	11°4.55′	119°39.65′	4436.5		
GSR	121	MUC	13°51.25′	123°15.3′	4517.7	30	
GSR	122	GC	13°51.23′	123°15.29′	4517.7	740	
GSR	128	BC	13°51.10′	123°15.12′	4510.7		
IFRE-1	165	GC	14°2.63′	130°8.39′	4922.7	927	
IFRE-1	167	MUC	14°2.62′	130°8.32′	4918.8	29	
IFRE-1	180	BC	14°2.50′	130°8.18′	4936.4		
IFRE-2	174	GC	14°2.44′	130°5.1′	5008	734	no nodules
IFRE-2	175	MUC	14°2.45′	130°5.11′	5005.5	36	
APEI3	194	GC	18°47.54′	128°22.33′	4815.5	576	
APEI3	195	BC	18°47.75′	128°21.73′	4833.4		
APEI3	199	MUC	18°47.46′	128°22.42′	4816.6	32	

3.1. Pore-water and sediment sampling

Immediately after core recovery, sediment cores were transferred into the cold room of the RV SONNE at a temperature of ~ 4 °C. Two MUC cores were separately used for (1) oxygen measurements and subsequent solid-phase sampling and (2) the retrieval of bottom water and pore water by means of rhizons with an average pore size of 0.1 µm (Seeberg-Elverfeldt et al., 2005). Pore water was sampled at intervals of 1 cm in the upper 10 cm and at 2 cm below. For solid-phase investigations the sample interval for the MUC cores was 1 cm.

The GCs were cut into 1 m segments on deck and stored in the cold room for at least 12 h in order to allow temperature equilibration of the sediments before oxygen measurements were performed. After the oxygen measurements, the segments were split into two halves from which the 'working half' was used for pore-water and sediment sampling while the other half was kept undisturbed and archived. Pore-water and sediment from the GCs were sampled every 20 cm.

During the pore-water sampling by rhizons, the first mL of extracted pore water was discarded in order to avoid any dilution or oxidation. Sample aliquots of typically 2 mL for nitrate (NO_3) were stored in amber vials sealed with a PTFE septum-bearing lid at − 20 °C. For the analyses of further dissolved pore-water constituents, aliquots of the remaining pore-water samples were diluted 1:10 and acidified with 0.145 M sub-boiling distilled HNO_3 and stored at 4 °C in Zinsser vials. All sediment samples were taken using either cut-off syringes with a volume of about 12 mL or with a plastic spatula and stored at − 20 °C in plastic vials. Sediment samples from suboxic intervals of the cores were stored in argon-flushed gas-tight glass bottles at − 20 °C until further analysis.

3.2. Ex situ oxygen measurements

Oxygen concentrations in the sediment were determined using amperometric Clark-type oxygen sensors with an internal reference and equipped with a guard cathode (Revsbech, 1989) according to the procedure described by Ziebis et al. (2012) and Mewes et al. (2014). The electrodes (Unisense, Denmark) are made of glass with a 6 cm long tip that was inserted into a hyperdermic needle (diameter 1.1 mm, length 50 mm) and had a response time shorter than 10 s. Signals were amplified and transformed to mV by a picoamperemeter, digitalized by an analogue/digital converter (ADC 216, Unisense, Denmark) and recorded using the software PROFIX (Unisense, Denmark). Measurements were recorded at each sampling point for 2–3 min and mean oxygen saturation values were taken when signals were stable to calculate the depth profiles. For the two-point calibration of the oxygen sensors, Ar-flushed (0% oxygen saturation) and air-purged (100% oxygen saturation) local bottom water was used. High-resolution (1 mm) vertical profiles of oxygen concentrations across the sediment/water interface were accomplished for MUC cores by use of a micromanipulator down to a maximum sediment depth of 5–6 cm. For oxygen measurements in deeper parts of the MUC core as well as for all GCs, holes were drilled through the walls of the core liners in intervals of 1 cm for MUCs and of 5 cm for GCs for the insertion of the microelectrode.

3.3. Pore-water analyses

In the home laboratory at the Alfred Wegener Institute Helmholtz Centre for Polar and Marine Research in Bremerhaven (AWI), NO_3^- was determined using a QuAAtro Continuous Segmented Flow Analyzer (Seal Analytical) with a detection limit of 1.9 µM. Based on duplicate measurements of NO_3^-, the accuracy of the analysis was determined to be < 4.9%. Dissolved manganese (Mn^{2+}) was determined in the acidified pore-water subsamples by inductively coupled plasma optical emission spectrometry (ICP-OES; IRIS Intrepid ICP-OES Spectrometer, Thermo Elemental) with a detection limit of 0.05 µM. Based on the triplicate determination of each sample the reproducibility was < 1.5% for Mn^{2+}.

3.4. Solid-phase analyses

To avoid any interference of the salt matrix in the pore water on the sediment composition, bulk sediment data, total organic carbon and total sulfur contents have been corrected post-analytically according to Kuhn (2013) with the mass percentage of the saline pore water (w') and the mass percentage of H_2O of the wet sediment (w) with the pore water containing 96.5% H_2O (Eq. (1)). With the mass of the salt s [%] (Eq. (2)) the solid-phase composition c' has been calculated using the measured solid-phase composition c (Eq. (3)).

$$w' = w*100/96.5 \tag{1}$$

$$s = 100*\frac{w' - w}{100-w} \tag{2}$$

$$c' = c*\frac{100}{100-s} \tag{3}$$

3.4.1. Total organic carbon content

The content of total organic carbon (TOC) was analyzed using an Eltra CS2000. About 100 mg of freeze-dried, homogenized sediment were weighed into a ceramic cup. Samples were decalcified with 0.5 mL 10% HCl at 250 °C for 2 h before analysis. As the total carbon (TC) consists mostly of TOC in the analyzed samples, total inorganic carbon (TIC) occurs only in negligible amounts. Based on an in-house reference material precision of the analysis was determined to be < 3.7% (n = 83).

3.4.2. Radioisotope analyses of ^{231}Pa and ^{230}Th

For the isotope dilution analysis by Inductively Coupled Plasma-Sector Field-Mass Spectrometry (ICP-SF-MS, Element2, Thermo Scientific) freeze-dried and homogenized sediment samples were spiked with about 9 pg ^{229}Th, 0.7 pg ^{233}Pa and 800 pg ^{236}U as internal standards and weighed out in Teflon vials. Total acid digestions were performed in the microwave system MARS Xpress (CEM) according to the procedure described by Kretschmer et al. (2010) and Nöthen and Kasten (2011). Acids were of sub-boiling distilled (HNO_3, HCl) or suprapur® (HF) quality. About 50 mg of freeze-dried and homogenized bulk sediment were digested in an acid mixture of 65% HNO_3 (3 mL), 30% HCl (2 mL) and 40% HF (0.5 mL) at ~ 230 °C. The digested solutions were fumed off to dryness with the microwave evaporation accessory (CEM XpressVap) and re-dissolved under pressure in 1 M HNO_3 (5 mL) at ~ 200 °C. The residue was filled up to 50 mL with 1 M HNO_3. After the total acid digestion, 80% of the total digest volume were co-precipitated with $Fe(OH)_3$. Separation of Pa, Th and U was performed by ion exchange chromatography with the Anion Exchange Resin AG® 1-X8 (Bio-Rad) after the protocols of Anderson and Fleer (1982) and Andersson and Schöberg (2012). Poly-Prep® gravity flow columns filled with AG® 1-X8 resin were conditioned with 9 M HCl (3 * 4 mL) before loading the sample and eluting Th with 9 M HCl (3 * 4 mL), Pa with 9 M HCl/0.14 M HF (4 * 3 mL) and U with 0.1 M HCl (4 * 3 mL), successively. All acids were of sub-boiling distilled or suprapur® quality. The Th, Pa and U eluates were collected and evaporated in Teflon beakers. The Th eluates were purified on a second column with 9 M HCl (400 µL and 6 * 2 mL) for Th, 9 M HCl/0.14 M HF (6 * 2 mL) for Pa and 0.1 M HCl (3 * 4 mL) for U. Separated Th, Pa and U fractions were evaporated, redissolved in HNO_3 and diluted to 1 M HNO_3 for the isotope dilution analysis using ICP-SF-MS with the desolvation system Apex Q (ESI). Data correction for the formation of thorium hydride ($^{232}ThH^+$), ^{232}Th peak tailing and the instrument mass bias were assessed as described by Kretschmer et al. (2011). Based on the reference material Urem-11 (SARM-31) average accuracy and precision were 0.5% and 1.2% for ^{235}U, 2.4% and 1.2% for ^{230}Th and 0.3% and 2.6% for ^{231}Pa, respectively (n = 5).

Sedimentation rates were calculated following the algorithm by Faure (1977), where t is the age[yr] of the sediment and $\frac{^{230}Th_{ex}}{^{231}Pa_{ex}}$ is the specific activity ratio at a certain sediment depth x. Here, we used the well constrained value in the bioturbated layer above (Supplementary Fig. 1) as the starting value b, respectively (Eq. (5)).

$$t = \frac{1}{82574.86} \ln \left[\frac{\left(\frac{^{230}Th_{ex}}{^{231}Pa_{ex}}\right)_x}{\left(\frac{^{230}Th_{ex}}{^{231}Pa_{ex}}\right)_b} \right] \tag{5}$$

Mass accumulation rates [g cm^{-2} kyr^{-1}] were determined by the product of sedimentation rate [cm kyr^{-1}] and dry bulk density (DBD) [g cm^{-3}].

3.5. Geochemical model setup and reaction network

A one-dimensional steady-state reaction transport model (e.g. Boudreau, 1997) that couples reactions through a discretized steady-state reaction-transport equation was used to interpret the sedimentary geochemistry at the various CCZ sites (Eq. (6)):

$$0 = \frac{\partial D_{i,j}\vartheta_i(\partial C_{i,j}/\partial z)}{\partial z} - \frac{\partial \omega_i \vartheta_i C_{i,j}}{\partial z} + \alpha_i \vartheta_i (C_{i,j} - C_{0,j}) + \vartheta_i \sum R_{i,j} \tag{6}$$

where z is sediment depth, and i, j represent subscripts depicting depth- and species-dependence, respectively. C is the species concentration (aqueous or solid species, Supplementary material Table 2); D is the diffusive mixing coefficient taking tortuosity (Boudreau, 1997) and bioturbation (Eq. (7)) into account ($D_i = B_i + D_{m,i}$); ϑ is the volume fraction for the aqueous (i.e. the porosity φ) or solid ($1 - \varphi$) phases; ω is

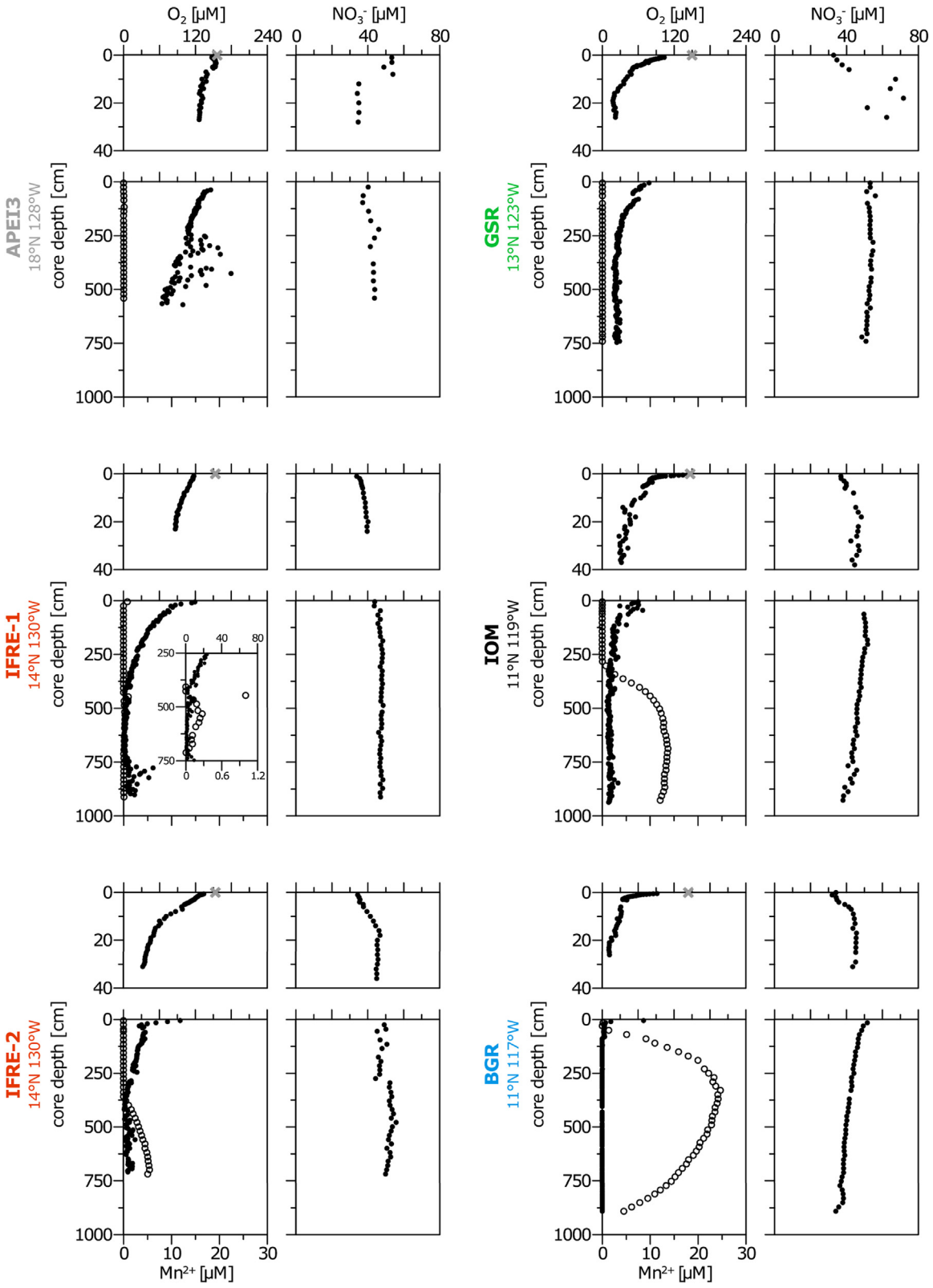

Fig. 2. Pore-water profiles of oxygen, dissolved Mn(II) and nitrate of the APEI3, IFREMER, GSR, IOM and BGR sites. The inset plot for the IFRE-1 site show oxygen (black dots) and dissolved Mn(II) concentrations (open circles) on separate axes (upper axis: oxygen; lower axis: Mn(II)) between 2.5 and 7.5 m sediment depth. Bottom-water oxygen concentrations measured by CTD are indicated (grey crosses).

the velocity of either the aqueous or the solid phase (v or w respectively); α_i is the bioirrigation coefficient (0 for solid species, Eq. (7)); $\sum R_{i,j}$ is the sum of the reactions affecting the given species j.

The reaction-transport model consists of 8 geochemical species and 6 reactions (Supplementary material Table 1):

$$(CH_2O)(NH_4^+)_{\frac{16}{106}} + O_2 \rightarrow CO_2 + \frac{16}{106}NH_4^+ + H_2O \quad \text{(R1)}$$

$$5(CH_2O)(NH_4^+)_{\frac{16}{106}} + 4NO_3^- + 4H^+ \rightarrow 2N_2 + 5CO_2 + 5\frac{16}{106}NH_4^+ + 7H_2O \quad \text{(R2)}$$

$$(CH_2O)(NH_4^+)_{\frac{16}{106}} + 2MnO_2 + 4H^+ \rightarrow 2Mn^{2+} + CO_2 + \frac{16}{106}NH_4^+ + 3H_2O \quad \text{(R3)}$$

$$2Mn^{2+} + O_2 + 2H_2O \rightarrow 2MnO_2 + 4H^+ \quad (R_4)$$

$$NH_4^+ + 2O_2 \rightarrow NO_3^- + 2H^+ + H_2O \quad \text{(R5)}$$

$$3MnO_2 + 2NH_4^+ + 4H^+ \rightarrow 3Mn^{2+} + N_2 + 6H_2O \quad \text{(R6)}$$

The chemical reactions during organic carbon degradation were assumed to follow the Redfield ratio stoichiometry with the organic-bound nitrogen to carbon ratio of 16:106 (Redfield, 1934). Biologically induced mixing profiles were assumed to follow a modified logistic function where the break attenuation depths were assumed to be the same for both bioirrigation and bioturbation:

$$B_i = B_0 \exp\left(\frac{z_{mix} - z}{z_{att}}\right) / \left(1 + \exp\left(\frac{z_{mix} - z}{z_{att}}\right)\right) \quad (7)$$

$$\alpha_i = \alpha_0 \exp\left(\frac{z_{mix} - z}{z_{att}}\right) / \left(1 + \exp\left(\frac{z_{mix} - z}{z_{att}}\right)\right) \quad (8)$$

where α_0 and B_0 are constants representing the maximum biorrigation and bioturbation coefficients at sediment-water interface, z_{mix} is the depth to where α_0 and B_0 become half their value and z_{att} is the attenuation of the biogenically induced mixing with depth.

Porosity data were fit for each station and showed an exponential decrease with depth typical of compacting sediment (not shown) and were fit with the following equation:

$$\varphi_i = \varphi_\infty(\varphi_0 - \varphi_\infty)\exp(-\beta z) \quad (9)$$

where φ_∞ is the porosity at compaction, φ_0 is the porosity at the sediment water interface, and β is the depth-attenuation coefficient. Sediment thicknesses for the diagenetic model were extracted from NCEI's global ocean sediment thickness grid (Whittaker et al., 2013). For the BGR site, sediment thicknesses were inferred from nearby core locations with similar pore-water Mn profiles (SO240-9KL, SO240-96SL; Kuhn et al., 2017). The model was coded in R (version 3.2.4) using the ReacTran package (Soetaert and Meysman, 2012) to solve Eq. (6) and the marelac package (Soetaert et al., 2010) to solve the molecular diffusion coefficients for the modeled species ($D_{m,i}$). The advective velocities of solid and pore water phases were solved using the compact grid function within the ReacTran package, which takes sedimentary compaction into account.

4. Results

4.1. Core description

All study sites show light brown clay-dominated siliceous ooze with variable surface nodule coverage (Table 1). The sediments in the APEI3 site are dominated by dense and dry, dark brown sediment with a comparably low degree of lithological variation. All other sites are characterized by light brown sediments with irregular dark patches and layers throughout.

4.2. Pore water

Bottom-water oxygen concentrations measured with the CTD (SBE 43 oxygen self-regenerative WetLabs Clark-sensor) are 156 μM in the APEI3 area, 153 μM in the IFREMER area, 150 μM in the GSR area, 147 μM in the IOM area and 144 μM in the BGR area (Fig. 2). In the surface sediments, oxygen concentrations usually decrease rapidly with depth in the upper 30 cm (Fig. 2). However, in contrast to the other sites, the surface sediments of the APEI3 and IFRE-1 sites show only a slight decrease in oxygen. Oxygen concentrations below detection limit are reached at various sediment depths while the sediments at the APEI3 and the GSR sites remain oxic throughout. The oxygen penetration depth (OPD) is 1 m at the BGR site, 3 m at the IOM site, 4.5 m at the IFRE-1 site and 3.8 m at the IFRE-2 site.

Pore-water Mn^{2+} occurs below the OPD within a wide concentration range of 0.2–25 μM (Fig. 2). At the IFRE-1 site, Mn^{2+} concentrations < 1 μM are between 4.5 and 7 m while the IFRE-2 site shows a concave-up profile with higher concentrations of up to 5.5 μM. At the IOM site, Mn^{2+} increases downward to 13 μM and slightly decreases below 8 m. Overall, the highest Mn^{2+} concentrations were measured at the BGR site with up to 25 μM at 3.3 m and a subsequent decrease in concentrations with depth.

NO_3^- concentrations generally increase with depth from bottom water concentrations of 35 μM at the sediment surface to 45 μM in the upper 30 cm (Fig. 2). The APEI3 and GSR sites show NO_3^- concentrations in the surface sediments of up to 53 μM and 70 μM, respectively. A decrease of NO_3^- with depth below 30 cm is detected at the BGR, IOM and IFRE-2 sites to about 35 μM at the bottom of the cores. At the APEI3, IFRE-1 and GSR sites, NO_3^- concentrations remain mostly constant throughout the deep sediment core.

4.3. Solid phase

4.3.1. Total organic carbon

The TOC contents generally decrease with depth in the upper 30 cm (Fig. 3). The lowest surface sediment TOC contents of 0.2 wt% are found in the APEI3. Both, the IFRE-1 and IFRE-2 sites, show 0.3–0.4 wt % of TOC while the GSR site and the IOM site have 0.5 wt% of TOC. The highest contents with 0.6 wt% are found at the BGR site. Below 30 cm, the TOC remains < 0.2 wt% (Fig. 3). A drop to TOC contents of < 0.1 wt% is found at the GSR site below 5 m sediment depth.

4.4. Sedimentation rates and bioturbation depth

Sedimentation rates range between 0.2 and 1.15 cm kyr^{-1} (Fig. 4). The rates at the APEI3 and the GSR sites are at least threefold lower than at the IFRE-1 and the IOM sites. Bioturbation is usually limited to the upper 7 cm whereas the bioturbated layer at the IOM site reaches down to 13 cm (Supplementary Fig. 1).

5. Discussion

5.1. POC flux to the seafloor and sedimentation rates

Pelagic deep-sea sediments receive little organic matter (OM) due to generally low surface water productivity and great water depth (Heath et al., 1977; Müller and Suess, 1979; Honjo, 1980). For the prediction of carbon export production at any water depth, Suess (1980) developed an empirical algorithm from sediment trap measurements and primary production (PP) rates in the respective surface waters. Several studies have applied modified algorithms after Suess (1980) (e.g., Dymond et al., 1997; Tyrell, 1999) and Martin et al. (1987) (e.g., Emerson et al., 1997; Fischer et al., 2000) for predicting the vertical POC flux. However, these commonly applied relationships between POC flux and water depth generally overestimate the flux of OM to depth (Buesseler et al., 2007; Buesseler and Boyd, 2009; Henson et al., 2011; Arndt et al., 2013 and references therein). Lutz et al. (2002) developed regional algorithms including region-specific sinking and remineralization rates, i.e. labile and refractory POC fractions in the water column. Using this empirical parameterization of the POC flux to depth, Lutz et al. (2007) combined a time series of remotely sensed net PP in the surface waters, sea surface temperature and sediment trap POC flux data to construct models with global predictions of POC fluxes to the seafloor. According to the model by Lutz et al. (2007), about 1.7 mg C_{org} m^{-2} d^{-1} is delivered

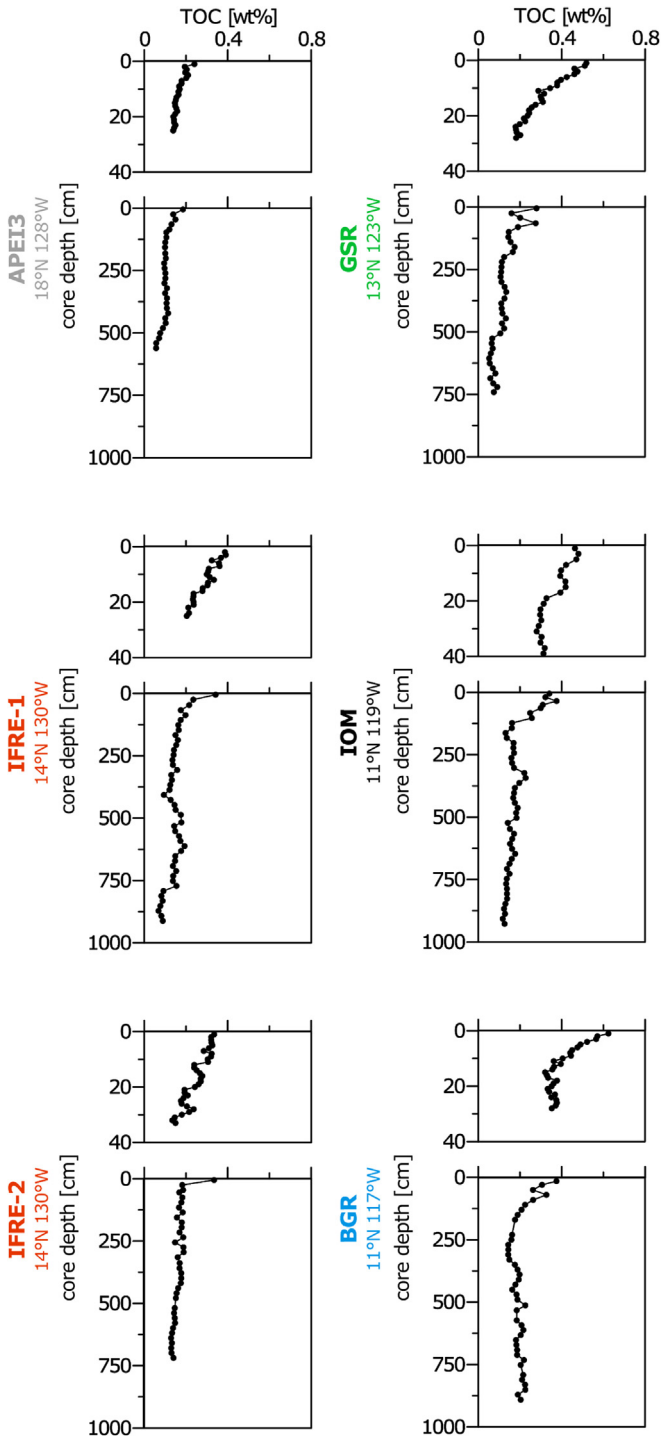

Fig. 3. Solid-phase profiles of TOC of the APEI3, IFREMER, GSR, IOM and BGR sites.

to the seafloor at the BGR and IOM sites, 1.5 mg C_{org} m^{-2} d^{-1} reaches the sediments of the GSR and IFREMER sites and 1.3 mg C_{org} m^{-2} d^{-1} settles to the seafloor in the APEI3 area (Fig. 1). These fluxes may be biased due to (1) significant uncertainties in the NPP estimates based on satellite data and (2) several potential errors in the trapping efficiency of sediment traps (Lutz et al., 2007 and references therein). Furthermore, with water depths of 4–5 km, the export production may be laterally drifted during settling, especially by strong bottom currents in the proximity of seamounts (e.g., Mewes et al., 2014). We implemented the POC fluxes given by Lutz et al. (2007), which can be regarded as rough estimates, into our reaction transport model and adjusted these values in order to fit the measured profiles of TOC and the oxidants. Our diagenetic model reproduces the Lutz et al. (2007) fluxes within 20% (Table 2). Only a slight discrepancy occurs between the POC fluxes derived from both models for the APEI3 and BGR sites. Compared to the other studied contract areas, the water column in the APEI3 area is characterized by a less pronounced OMZ (Martínez Arbizu and Haeckel, 2015). Thus, due to the significantly longer oxygen exposure time of settling POC, which is the key parameter determining the degradation efficiency of POC (e.g. Hartnett et al., 1998; Banse, 1990; Zonneveld et al., 2010; Cavan et al., 2017), the degradation in the water column may be enhanced in this area. The regional differences in the OMZ thickness may limit the empirical algorithm used by Lutz et al. (2007) for calculating the POC flux to the seafloor. Thus, POC fluxes in the APEI3 area are most likely overestimated. Conversely, the POC flux in the BGR area has likely been underestimated as the water column is characterized by an extensive OMZ (Martínez Arbizu and Haeckel, 2015) aiding the POC preservation in the water column and triggering a higher POC flux to the sediment (Table 2). This is consistent with our 20% lower fluxes at the APEI3 site and 20% higher POC flux at the BGR site in comparison with the Lutz et al. (2007) fluxes.

Although considerably higher estimated POC fluxes between 1.5 and 11.5 mg C_{org} m^{-2} d^{-1} have been reported from nearby stations (Murray and Kuivila, 1990; Mogollón et al., 2016), the TOC contents at the sediment surface at all sites are mostly in agreement with published values from the CCZ ranging from 0.1 to 0.6 wt% (Müller, 1977; Müller and Mangini, 1980; Jahnke et al., 1982; Murray and Kuivila, 1990; Mewes et al., 2014, 2016). Mewes et al. (2014) have presented geochemical data for sediments from the BGR contract area "East" with two sites close (< 5 km) to a large seamount between the BGR and IOM area (A1-1-MN, A1-2-NN) and two sites far away from seamounts (A5-1-BN, A5-2-SN). While the surface sediment TOC contents are similar at all stations, a comparably rapid decrease in TOC contents with depth occurs at the sites adjacent to the seamount with relatively high POC fluxes of 10 mg C_{org} m^{-2} d^{-1} (Fig. 6; Mogollón et al., 2016). Our BGR site shows up to 20% higher TOC contents in the upper 30 cm than the sites studied by Mewes et al. (2014) which also decrease rapidly with sediment depth (Fig. 6). Khripounoff et al. (2006) reported 25% higher TOC contents in the upper 30 cm at a site in the IFREMER area (Fig. 6). Variations in local estimated POC fluxes, TOC contents and sedimentation rates are potentially a result of strong local heterogeneities of bottom water currents which can be intensified, attenuated and deflected in the vicinity of seamounts and ridges (Hogg, 1973; Gould et al., 1981; Mohn and Beckmann, 2002; Xu and Lavelle, 2017; Juan et al., 2018) and cause kilometer-scale differences in the supply and composition of sediments (Turnewitsch et al., 2004, 2015; Mewes et al., 2014). The relatively high sedimentation rates at the IOM site of 1.15 cm^{-1} kyr^{-1} may be associated with sediment focusing. Furthermore, sediments of different composition may be delivered from the slopes of nearby seamounts and ridges by gravity-induced processes (e.g., Stanley and Taylor, 1977; Jeong et al., 1994).

5.2. Organic matter degradation

Müller et al. (1988) have suggested that aerobic respiration is the dominant biogeochemical process degrading sedimentary OM in the CCZ and previous modeling studies for the BGR contract area "East" (Table 2; Fig. 5; Mewes et al., 2016; Mogollón et al., 2016) have supported this assumption. Our model simulations are in line with these findings and show that aerobic respiration consumes more than 90% of the OM delivered to the seafloor while denitrification and Mn(IV) reduction together consume less than 1%. These numbers agree well with rates derived from the previous modeling studies for the BGR contract area "East" (Table 2; Fig. 5; Mogollón et al., 2016; Mewes et al., 2016). The zone in which manganese and nitrate reduction co-occur will hereafter be referred to as "suboxic zone" in which neither oxygen nor hydrogen sulfide are present (Berner, 1981). Most of the ammonia

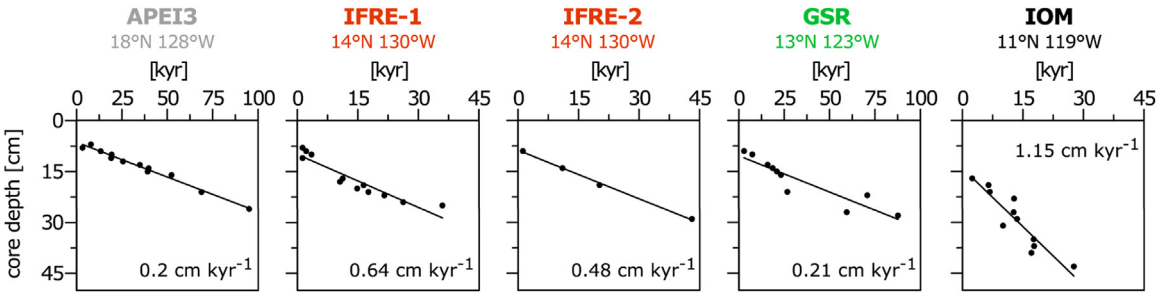

Fig. 4. $^{230}Th/^{231}Pa$-derived sedimentation rates for the uppermost 50 cm of the sediments of the APEI3, IFREMER, GSR and IOM sites.

Table 2
Fluxes of POC and oxygen into the sediment and depth-integrated rates of the predominant biogeochemical processes derived from the diagenetic model.

Biogeochemical process	Unit	BGR	IOM	GSR	IFRE-1	IFRE-2	APEI3
POC flux	[mg C m^{-2} d^{-1}]	1.99	1.54	1.51	1.47	1.5	1.07
O_2 flux top	[mg O_2 m^{-2} d^{-1}]	5.18	4.24	3.61	4.3	4.37	2.58
O_2 reduction	[mg C m^{-2} d^{-1}]	1.92	1.44	1.38	1.3	1.45	0.93
NO_3^- reduction	[mg C m^{-2} d^{-1}]	1.5E−03	1.7E−03	3.3E−02	5.5E−03	5.0E−03	8.7E−04
Mn(IV) reduction	[mg C m^{-2} d^{-1}]	1.5E−03	6.1E−04	1.6E−02	5.7E−04	4.6E−03	1.4E−03
Nitrification	[mg N m^{-2} d^{-1}]	0.01	0.13	0.14	0.10	0.14	0.03
Mn^{2+} oxidation	[mg O_2 m^{-2} d^{-1}]	0.062	0.026	0.06	0.025	0.029	0.016
Mn-annamox	[mg Mn m^{-2} d^{-1}]	0.14	0.005	0	0	0	0

liberated from OM degradation becomes nitrified in the oxic zone so that the nitrate concentrations increase with depth in the upper 30 cm of sediment (Fig. 2; Fig. 5). Additionally to nitrification, the breakup of nitrate-rich organic compounds may contribute to the relatively high NO_3^- concentrations in the surface sediments at the APEI3 and GSR sites (e.g., Jørgensen and Gallardo, 1999). The bioturbated layer includes the upper 6–13 cm of the oxic sediment which is in good agreement with the average bioturbation depth of 10 cm (Boudreau, 1994). The determined low sedimentation rates of 0.2–1.15 cm kyr^{-1} in combination with low POC fluxes to the seafloor (< 2 mg C_{org} m^{-2} d^{-1}) lead to low carbon burial rates of less than 0.15 mg C_{org} m^{-2} d^{-1} (based on depth-integrated rates, cf. Table 2), which are consistent with other organic carbon burial estimates for the CCZ (e.g., Jahnke, 1996). The highly refractory TOC fraction of < 0.2 wt% below 20 cm is insufficient to reduce nitrate (Table 2; Fig. 5; Supplementary Table 2; Mogollón et al., 2016). These observations are in agreement with Müller and Mangini (1980) and Müller et al. (1988) who state that with sedimentation rates of 0.2–0.4 cm kyr^{-1} OM is almost completely remineralized within the uppermost meter of the sediments. Mewes et al. (2014) determined carbon respiration rates for sediments in the BGR contract area "East" that showed twofold higher respiration rates in the upper oxic sediments compared to the depth-integrated rates of aerobic respiration derived from our diagenetic model (Table 2). This offset may be caused by the alteration of the microbial communities during sediment retrieval, i.e. decompression (e.g., Park and Clark, 2002), and the different approaches of respiration rate determination. Moreover, the discrepancy in the respiration rates may reflect the lateral heterogeneity in the supply of TOC related to the interaction of currents with rough seafloor topography, in particular seamounts. Twofold higher rates of aerobic respiration at the BGR site compared to the APEI3 site are a result of twofold higher POC fluxes to the seafloor at the BGR site than at the APEI3 site in the proximity of the carbon-starved North Pacific gyre. Consequently, the APEI3 site does not represent the (bio) geochemical conditions of the sites in the European contract areas investigated in the framework of this study. This observation is in agreement with Vanreusel et al. (2016) who explained the significantly lower faunal densities in the APEI3 with primary productivity being much lower compared to in the contract areas.

5.3. Redox zonation and oxygen fluxes

The *ex situ* sediment oxygen concentrations are in good agreement with other oxygen data for the equatorial Pacific Ocean (Murray and Grundmanis, 1980; Jahnke et al., 1982; Berelson et al., 1990; Hammond et al., 1996; Khripounoff et al., 2006; Mewes et al., 2014, 2016; Rühlemann et al., 2011). In accordance with oxygen measurements by Mewes et al. (2014), bottom water oxygen measurements of the overlying water of the MUC cores using amperometric Clark-type oxygen sensors are systematically 10–20% higher than bottom-water concentrations determined with the CTD 20–30 m above the seafloor (Martínez Arbizu and Haeckel, 2015). This offset is most likely a result of sampling artifacts that occurred during retrieval of the MUC cores or of atmospheric oxygen diffusion into the bottom water of the surface sediments during *ex situ* measurements, which biases the oxygen concentrations down to about 0.4 cm sediment depth. The threshold of 0.4 cm has been determined in this study by triplicate profiling across the water-sediment interface resulting in systematically higher oxygen concentrations of each consecutively measured profile. Therefore, we excluded oxygen concentrations in the uppermost 0.4 cm from the calculation of oxygen gradients and fluxes and used the CTD oxygen concentrations as bottom water values (Table 2; Table 3). The oxygen data obtained for the IOM site indicate that oxygen is not completely depleted throughout the sediment core (Fig. 2). However, the detection of dissolved Mn^{2+} in pore water below 3 m sediment depth suggests that oxygen is absent in this interval. We attribute this discrepancy to some calibration problems of one of the sensors at the beginning of the cruise which affected the oxygen measurements at the BGR and IOM sites. Additionally, the discrepancy between the GSR oxygen concentrations of the MUC and the GC is attributed to small-scale variations or to miscalibration of the oxygen sensor. Even though the oxygen data shows sampling artifacts and miscalibration, which partly bias the absolute oxygen concentrations, it can be used in combination with the pore-water Mn^{2+} data to delineate the sedimentary redox zonation. As the oxygen data at the bottom water-sediment interface is particularly affected, oxygen fluxes into the sediment are given with an error of < 5%.

The OPD inversely correlates with the POC flux (r^2 = 0.85; Fig. 7). The OPD of 1 m at the BGR site is shallower than the OPD reported for other sites studied in this region which range between 1.8 and 3 m

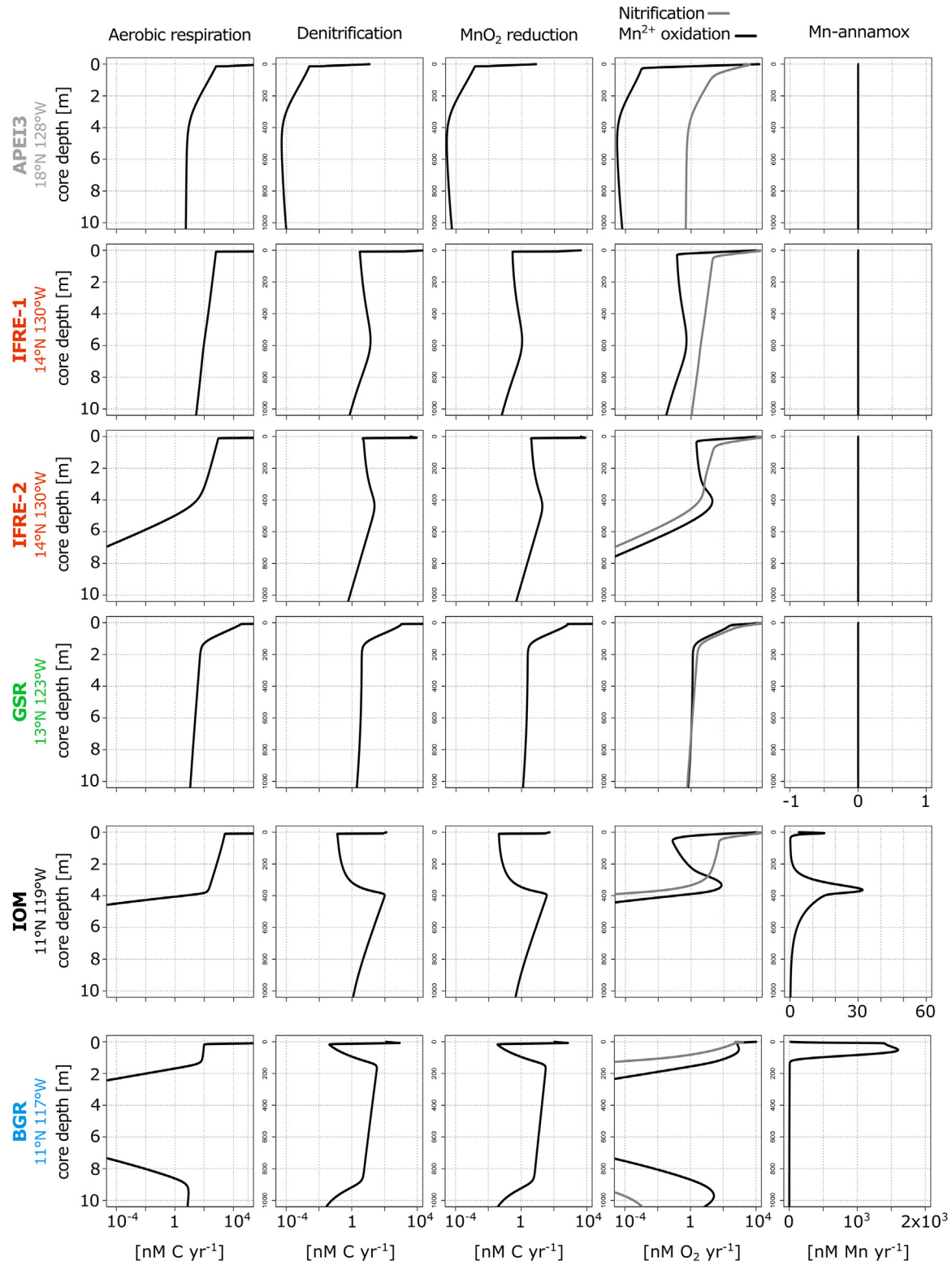

Fig. 5. Model results for all sites including the biogeochemical processes of aerobic respiration, Mn(IV) reduction, denitrification, Mn^{2+} oxidation, nitrification and Mn-annamox (R_1-R_6).

depth (Rühlemann et al., 2011; Mewes et al., 2014). Such small-scale variation is reflected in the oxygen gradients with 2.6–5.6 μM O_2 mm^{-1} in the sediments in the BGR area (Table 3). OPDs are generally deeper at sites with medium-sized or big (3–10 cm) nodules at the sediment surface than at sites with small-size (1–8 cm) or without nodules at the surface (Mewes et al., 2014). The two IFREMER sites (IFRE-1 and IFRE-2) are ~ 6 km apart with medium-sized surface nodules at the IFRE-1 site and no nodules at the IFRE-2 site (Table 1) and in accordance with the findings of Mewes et al. (2014), the OPD at the IFRE-1 site is located 70 cm deeper than at the IFRE-2 site (Fig. 2). However, the depth-integrated rates of Mn(IV) and nitrate reduction are not significantly higher at the IFRE-2 site compared to the IFRE-1 site (Table 2; Fig. 5)

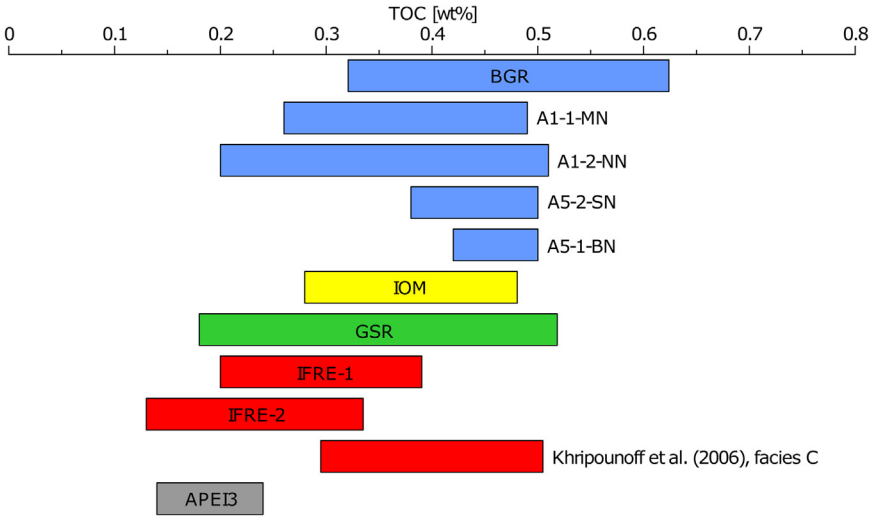

Fig. 6. Comparison of the TOC contents of surface sediments (upper 30 cm) within the different contract areas CCZ. The data for the BGR sites A1-1-MN, A1-2-NN, A5-2-SN, A5-1-BN from cruise SO205 are taken from Mewes et al. (2014). The range of TOC contents comprises the lowest to highest measured contents throughout MUC cores taken at the individual sites. The highest TOC content at each site was determined at the sediment surface, i.e. in the uppermost centimeter of the sediment.

Table 3
Oxygen gradients calculated from oxygen profiles for the uppermost 0.4–1 cm of sediment. Negative gradients indicate the oxygen flux into the sediment. The data from SO205 were taken from Mewes et al. (2014). Note that the oxygen gradient at the GSR site is biased due to miscalibration of the sensor.

Station	Oxygen gradient [µM mm^{-1}]
SO205–05MUC	− 3.5
SO205–06MUC	− 2.6
SO205–46MUC	− 5.6
SO205–48MUC	− 9
BGR	− 5
IOM	− 7
GSR	− 8.3
IFRE-1	− 3.5
IFRE-2	− 1.7
APEI3	− 0.2

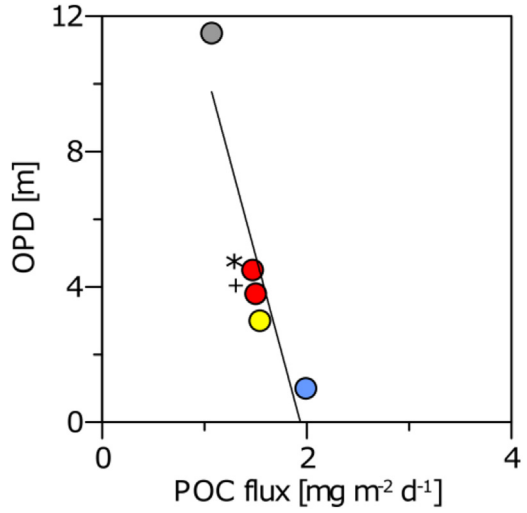

Fig. 7. Correlation between the oxygen penetration depth (OPD) and the POC fluxes used as boundary conditions for the diagenetic model. Based on interpolation of the oxygen profile at the APEI3 site, oxygen may be consumed at 11.5 m. The linear regression through the BGR (blue), IOM (yellow), *IFRE-1 (red), $^{+}$IFRE-2 (red) and APEI3 (grey) sites shows a coefficient of determination of $r^2 = 0.85$.

which disagrees with the results presented by Mewes et al. (2014). This discrepancy may be connected to almost twofold higher sedimentation rates proposed by the authors for the nodule-free sites compared to the sites with medium-sized/big nodules while in the IFREMER area, sedimentation rate at the IFRE-1 site exceeds the rate at the IFRE-2 site. In accordance with the low respiration rates at the APEI3 site, the oxygen gradient over the upper 0.4–1 cm of sediment is low at 0.2 µM O_2 mm^{-1} (Table 3). At depth, oxygen concentrations are scattered at the APEI3 site. We interpret this as an analytical artifact because the sediments at the APEI3 site were very dry and consolidated and have therefore very likely impacted the sensor measurements.

In the suboxic zone, Mn^{2+} concentrations between 0.2 and 25 µM agree well with reported values in the CCZ (Emerson et al., 1980; Jahnke et al., 1982; Mewes et al., 2014). Mn^{2+} is mainly mobilized by the dissimilatory reduction of Mn(IV) phases below the OPD (Figs. 2 and 5). As proposed by Mogollón et al. (2016) for adjacent sites, the observed concomitant decrease of nitrate in the suboxic zone of the sediment core from the BGR area suggests that the biogeochemical cycles of manganese and nitrogen are coupled. Excess ammonium produced by OC degradation in the oxic zone may escape aerobic nitrification and diffuse downwards into the suboxic zone where it can act as electron donor during manganese oxide reduction (Mn-annamox, Luther et al., 1997). Mn-annamox may induce the liberation of Mn^{2+} into the pore water of the sediments of the BGR and IOM sites with reaction rates similar to the rates published by Mogollón et al. (2016) (Table 2; Fig. 5). The nitrate concentrations determined within the framework of this study are in correspondence with previously published nitrate pore-water data from the CCZ ranging from 30 to 70 µM (Jahnke et al., 1982; Jeong et al., 1994; Mewes et al., 2014, 2016; Mogollón et al., 2016). Nitrate reduction is very weak at these sites due to the low and refractory OM content (Table 2). Iron and manganese oxidation coupled to nitrate reduction is probably also not feasible due to the low Mn^{2+} concentrations and Fe^{2+} levels below detection limit.

5.3.1. *Deep Mn^{2+} oxidation*

Decreasing-with-depth profiles of Mn^{2+} at the IFRE-1, IOM and BGR sites indicate that Mn^{2+} is consumed by either precipitation of an authigenic carbonate mineral (e.g., Gingele and Kasten, 1994) or by oxidation at depth (Fig. 2). Due to the fact that alkalinity is low in these sediments (data not shown), and thus, precipitation of a Mn carbonate phase is unlikely, we suggest that at depth, Mn^{2+} is most likely oxidized by oxygen diffusing from the underlying basaltic basement. Such upward diffusive supply of oxygen from oxic seawater circulating in the oceanic crust was first shown for the German contract area “East” by Mewes et al. (2016) and has recently been documented to be

widespread in the area by Kuhn et al. (2017). At the IFRE-1 site, Mn^{2+} is consumed at 7 m depth. Based on interpolation of the Mn^{2+} profiles, Mn^{2+} is reoxidized at ~ 9.25 m depth at the BGR site while it is consumed at ~ 20 m depth at the IOM site. The low-temperature circulation of seawater through the basaltic crust (e.g., Fisher and Wheat, 2010; Ziebis et al., 2012) underlying the sediments of the CCZ had so far only been shown for the BGR area "East" on the base of increasing-with-depth oxygen and decreasing-with-depth Mn^{2+} profiles (Mewes et al., 2016; Kuhn et al., 2017). Numerous seamounts and faults in the eastern CCZ have been shown to facilitate the recharge and subsequent discharge of oxic seawater into and from oceanic crust and diffusion of oxygen into the overlying sediments. The BGR, IOM, and IFRE-1 sites are located about 5 km, 3 km and 1 km, respectively from the adjacent ridge flanks (Fig. 1). At these sites, the sediment drape thicknesses range between 20 and 83 m (Supplementary Table 2). In comparison, the sites studied by Kuhn et al. (2017) in the BGR area had an average sediment thickness of 48 m. The Mn^{2+} profile at the IFRE-2 site does not indicate Mn^{2+} oxidation at depth while the sediments at the APEI3 and GSR sites are oxic throughout. The extended oxic zones at the APEI3 and GSR sites probably result from low organic carbon supply and respiration (Table 2), which is insufficient to fully consume the oxygen diffusing into the sediment from both the overlying seawater and the underlying basaltic crustal fluids. However, the retrieved core lengths of up to 7.5 m do not allow the identification of deep oxidative processes at these locations. Based on our pore-water data, widespread deep Mn^{2+} oxidation occurs at three sites of various contract areas within the CCZ.

6. Conclusion

We studied six abyssal sites in the Clarion-Clipperton Zone of five European contract areas for the exploration of polymetallic nodules and one site in an Area of Particular Environmental Interest (APEI3) over a distance of about 1300 km. The sites differ in POC fluxes to the seafloor (1–2 mg C_{org} m^{-2} d^{-1}) and sedimentation rates (0.2–1.15 cm kyr^{-1}) while the bioturbation depth is mostly limited to the upper 7 cm of the sediment. Solid-phase contents, pore-water profiles and the applied transport reaction model demonstrate significant inter-areal differences in sedimentation rates, the extension of oxic and suboxic zones and rates of organic matter remineralization. We show that the observed variability in redox zonation at the study sites is determined by differences in (1) surface water productivity and associated POC flux to the seafloor, (2) sediment accumulation rate and (3) the oxidation of pore-water Mn^{2+} at depth. Diagenetic modeling indicates that due to the low sedimentation rates, the labile fractions of organic carbon are restricted to the upper 20 cm of the sediment where OC degradation is dominated (90%) by aerobic respiration. Mn(IV) reduction and denitrification each consume less than 1% of the refractory organic matter. The suboxic zone is characterized by a wide range of Mn^{2+} concentrations where the sites with the highest POC fluxes indicate further production of Mn^{2+} by Mn-annamox. Mn^{2+}-mediated denitrification is absent at all sites due to insufficient Mn^{2+} concentrations. Downward decreasing Mn^{2+} concentrations at three sites indicate the widespread oxidation of Mn^{2+} at depth throughout the CCZ. Due to very low POC fluxes of 1 mg C_{org} m^{-2} d^{-1} to the seafloor in the APEI3 area, respiration rates at this site are about twofold lower than in the investigated European contract areas. Consequently, we infer that the preservation area APEI3 does not represent the depositional conditions and biogeochemical processes that are dominating in the investigated European contract areas. The POC fluxes to the seafloor and the sedimentation rates generally correlate with surface water productivity, however, within a given contract area, small-scale spatial (intra-areal) variations in geochemical conditions and biogeochemical processes are caused by (1) various extents of POC degradation processes in the water column and (2) small-scale interactions of bottom water currents and topography affecting the sedimentation pattern.

This study represents the first biogeochemical baseline study that advances our knowledge about regional variations of natural depositional and geochemical conditions as well as biogeochemical processes in the sediments of the vast deep-sea area of the CCZ. Our findings may deliver important baseline data to be used for the assessment of the impact of potential deep-sea mining activities. They will also serve as an input for the further development of the Environmental Management Plan by the International Seabed Authority (ISA).

Acknowledgements

We thank captain Lutz Mallon, the crew and the scientific party of RV SONNE cruise SO239 for the technical and scientific support. Thanks to Jennifer Ciomber, Benjamin Löffler and Vincent Ozegowski for their participation in onboard sampling and analysis. For analytical support in the home laboratory and during data evaluation we are grateful to Ingrid Stimac, Olaf Kreft, Dennis Köhler, Ingrid Dohrmann and Dr. Gerhard Kuhn (all at AWI). For providing the bathymetric grids we thank Prof. Dr. Jens Greinert (GEOMAR). Special thanks to Dr. Matthias Haeckel (GEOMAR), Prof. Dr. Gerhard Bohrmann (MARUM, University of Bremen), Dr. Timothy G. Ferdelman (MPI Bremen) and Dr. Gerard Versteegh for much appreciated discussions. We thank the four reviewers for their helpful comments that have improved this manuscript.

This study is funded by the German Federal Ministry of Education and Research (BMBF) in the framework of the JPI Oceans project MiningImpact (grant no. 03F0707G) as part of the JPI-Oceans pilot action EcoMining-DEU – Ecological Aspects of Deep-Sea Mining. Dr. José M. Mogollón was partially funded by the Netherlands Earth System Science Centre (NESSC). We acknowledge further financial support from the Helmholtz Association (Alfred Wegener Institute Helmholtz Centre for Polar and Marine Research). The data are available via the data management portal OSIS-Kiel and the geological data network PANGAEA.

Appendix A. Supporting information

Supplementary data associated with this article can be found in the online version at doi:10.1016/j.dsr.2018.08.006.

References

Anderson, R.F., Fleer, A.P., 1982. Determination of natural actinides and plutonium in marine particulate material. Anal. Chem. 54, 1142–1147. https://doi.org/10.1021/ac00244a030.

Andersson, P.S., Schöberg, H., 2012. Determination of 232Th and 230Th in seawater using a chemical separation procedure and thermal ionization mass spectrometry. Limnol. Oceanogr. Methods 10, 296–303. https://doi.org/10.4319/lom.2012.10.296.

Arndt, S., Jørgensen, B.B., LaRowe, D.E., Middelburg, J.J., Pancost, R.D., Regnier, P., 2013. Quantifying the degradation of organic matter in marine sediments: a review and synthesis. Earth-Sci. Rev. 123, 53–86. https://doi.org/10.1016/j.earscirev.2013.02.008.

Arrhenius, G., 1952. Sediment cores from the East Pacific. Elanders boktryckeri aktiebolag, Göteburg.

Banse, K., 1990. New views on the degradation and disposition of organic particles as collected by sediment traps in the open sea. Deep-Sea Res. Part A: Oceanogr. Res. Pap. 37 (7), 1177–1195.

Bender, M.L., 1983. The Manganese Nodule Program. Eos Trans. 64. AGU, pp. 42–43. https://doi.org/10.1029/EO064i005p00042.

Berelson, W.M., Hammond, D.E., Cutter, G.A., 1990. In situ measurements of calcium carbonate dissolution rates in deep-sea sediments. Geochim. Cosmochim. Acta 54, 3013–3020. https://doi.org/10.1016/0016-7037(90)90118-5.

Berger, W.H., 1974. Deep-sea sedimentation. In: Burk, C.A., Drake, C.L. (Eds.), The Geology of Continental Margins. Springer, New York, pp. 213–241.

Berner, R.A., 1981. A new geochemical classification of sedimentary environments. J. Sediment. Res. 51, 359–365.

Bischoff, J.L., Piper, D.Z., 1979. Marine Geology and Oceanography of the Pacific Manganese Nodule Province. Springer, New York.

Boudreau, B.P., 1994. Is burial velocity a master parameter for bioturbation? Geochim. Cosmochim. Acta 58, 1243–1249.

Boetius, A., Haeckel, M., 2018. Mind the seafloor. Science 359 (6371), 34–36. https://doi.org/10.1126/science.aap7301.

Boudreau, B.P., 1997. A one-dimensional model for bed-boundary layer particle exchange. J. Mar. Syst. 11, 279–303. https://doi.org/10.1016/S0924-7963(96)00127-3.

Buesseler, K.O., Boyd, P.W., 2009. Shedding light on processes that control particle export and flux attenuation in the twilight zone of the open ocean. Limnol. Oceanogr. 54, 1210–1232.

Buesseler, K.O., Antia, A.N., Chen, M., Fowler, S.W., Gardner, W.D., Gustafsson, O., Harada, K., Michaels, A.F., Rutgers van der Loeff, M., Manmohan, S., Steinberg, D.K., Trull, T., 2007. An assessment of the use of sediment traps for estimating upper ocean particle fluxes. J. Mar. Res. 65, 345–416.

Calvert, S.E., Price, N.B., 1977. Geochemical variation in ferromanganese nodules and associated sediments from the Pacific Ocean. Mar. Chem. 5, 43–74.

Cavan, E.L., Trimmer, M., Shelley, F., Sanders, R., 2017. Remineralization of particulate organic carbon in an ocean oxygen minimum zone. Nat. Commun. 8, 14847. https://doi.org/10.1038/ncomms14847.

Chun, C., 1908. Manganknollen. In: Wissenschafliche Ergebnisse der Deutschen Tiefsee-Expedition auf dem Dampfer "Valdivia" 1898–1899. pp. 111–114.

Craig, J.D., 1979. The relationship between bathymetry and ferromanganese deposits in the north equatorial Pacific. Mar. Geol. 29, 165–186. https://doi.org/10.1016/0025-3227(79)90107-5.

D'Hondt, S., Jørgensen, B.B., Miller, D.J., Batzke, A., Blake, R., Cragg, B.A., Cypionka, H., Dickens, G.R., Ferdelman, T., Hinrichs, K.-U., Holm, N.G., Mitterer, R., Spivack, A., Wang, G., Bekins, B., Engelen, B., Ford, K., Gettemy, G., Rutherford, S.D., Sass, H., Skilbeck, C.G., Aiello, I.W., Guèrin, G., House, C.H., Inagaki, F., Meister, P., Naehr, T., Niitsuma, S., Parkes, R.J., Schippers, A., Smith, D.C., Teske, A., Wiegel, J., Padilla, C.N., Acosta, J.L.S., 2004. Distributions of microbial activities in deep subseafloor sediments. Science 306, 2216–2221. https://doi.org/10.1126/science.1101155.

Dymond, J., Collier, R., McManus, J., Honjo, S., Manganini, S., 1997. Can the aluminium and titanium contents of ocean sediments be used to determine the paleoproductivity of the oceans? Paleoceanography 12, 586–593.

Emerson, S., Jahnke, R., Bender, M., Froelich, P., Klinkhammer, G., Bowser, C., Setlock, G., 1980. Early diagenesis in sediments from the eastern equatorial Pacific, I. Pore water nutrient and carbonate results. Earth Planet. Sci. Lett. 49, 57–80. https://doi.org/10.1016/0012-821X(80)90150-8.

Emerson, S., Quay, P., Karl, D., Winn, C., Tupas, L., Landry, M., 1997. Experimental determination of the organic carbon flux from open-ocean surface waters. Nature 389, 951–954.

Faure, G., 1977. Principles of Isotope Geology. Wiley.

Fischer, G., Ratmeyer, V., Wefer, G., 2000. Organic carbon fluxes in the Atlantic and the Southern Ocean: relationship to primary production compiled from satellite radiometer data. Deep-Sea Res. Part II 47, 1961–1997.

Fisher, A.T., Wheat, C.G., 2010. Seamounts as conduits for massive fluid, heat, and Solute Fluxes on Ridge Flanks. Oceanography 23, 74–87.

Gingele, F.X., Kasten, S., 1994. Solid-phase manganese in Southeast Atlantic sediments: implications for the paleoenvironment. Mar. Geol. 121, 317–332.

Glover, A.G., Smith, C.R., Paterson, G.L.J., Wilson, G.D.F., Hawkins, L., Sheader, M., 2002. Polychaete species diversity in the central Pacific abyss: local and regional patterns and relationships with productivity. Mar. Ecol. Prog. Ser. 240, 157–170. https://doi.org/10.3354/meps240157.

Gould, W.J., Hendry, R., Huppert, H.E., 1981. An abyssal topographic experiment. Deep-Sea Res. 28A, 409–440.

Greinert, J., 2016. Swath sonar multibeam EM122 bathymetry during SONNE cruise SO239 with links to raw data files. PANGAEA (pangaea.de/10.1594/PANGAEA.859456).

Halbach, P., Friedrich, G., von Stackelberg, U. (Eds.), 1988. The Manganese Nodule Belt of the Pacific Ocean. Enke, Stuttgart.

Hammond, D.E., McManus, J., Berelson, W.M., Kilgore, T.E., Pope, R.H., 1996. Early diagenesis of organic material in equatorial Pacific sediments: stoichiometry and kinetics. Deep-Sea Res. Part II: Top. Stud. Oceanogr. 43, 1365–1412. https://doi.org/10.1016/0967-0645(96)00027-6.

Hartnett, H.E., Keil, R.G., Hedges, J.I., Devol, A.H., 1998. Influence of oxygen exposure time on organic carbon preservation in continental margin sediments. Nature 391, 572–575.

Heath, G.R., Moore, T.C., Dauphin, J.P., 1977. Organic carbon in deep-sea sediments. In: Anderson, N.R., Malanioff, A. (Eds.), The Fate of Fossil Fuel CO_2 in the Oceans. Plenum Press, New York, pp. 605–625.

Henson, S.A., Sanders, R., Madsen, E., Morris, P.J., Le Moigne, F., Quartly, G.D., 2011. A reduced estimate of the strength of the ocean's biological carbon pump. Geophys. Res. Lett. 38, L04606. https://doi.org/10.1029/2011GL046735.

Hogg, N.G., 1973. On the stratified Taylor column. J. Fluid Mech. 58, 517–537.

Honjo, S., 1980. Material fluxes and modes of sedimentation in the mesopelagic and bathypelagic zones. J. Mar. Res. 38, 53–97.

International Seabed Authority (ISA), 2010. A Geological Model for Polymetallic Nodule Deposits in the Clarion-Clipperton Fracture Zone. Technical Study 6, Kingston, p. 211.

Jahnke, R.A., 1996. The global ocean flux of particulate organic carbon: areal distribution and magnitude. Glob. Biogeochem. Cycles 10, 71–88.

Jahnke, R.A., Emerson, S.R., Murray, J.W., 1982. A model of oxygen reduction, denitrification, and organic matter mineralization in marine sediments1. Limnol. Oceanogr. 27, 610–623. https://doi.org/10.4319/lo.1982.27.4.0610.

Jeong, K.S., Kang, J.K., Chough, S.K., 1994. Sedimentary processes and manganese nodule formation in the Korea Deep Ocean Study (KODOS) area, western part of Clarion-Clipperton fracture zones, northeast equatorial Pacific. Mar. Geol. 122, 125–150. https://doi.org/10.1016/0025-3227(94)90208-9.

Johnson, D.A., 1972. Ocean-floor erosion in the Equatorial Pacific. Geol. Soc. Am. Bull. 83, 3121–3144. https://doi.org/10.1130/0016-7606(1972)83[3121:OEITEP]2.0.CO;2.

Jones, D.O.B., Kaiser, S., Sweetman, A.K., Smith, C.R., Menot, L., Vink, A., 2017. Biological responses to disturbance from simulated deep-sea polymetallic nodule mining. PLoS One 12 (2). https://doi.org/10.1371/journal.pone.0171750. (e0171750).

Jørgensen, B.B., Gallardo, V.A., 1999. *Thioploca spp.*: filamentous sulfur bacteria with nitrate vacuoles. FEMS Microbiol. Ecol. 28, 301–313.

Juan, C., Van Rooij, D., De Bruycker, W., 2018. An assessment of bottom current controlled sedimentation in Pacific Ocean abyssal environments. Mar. Geol. 403, 20–33.

Kalvelage, T., Lavik, G., Jensen, M.M., Revsbech, N.P., Löscher, C., Schunck, H., Desai, D.K., Hauss, H., Kiko, R., Holtappels, M., LaRoche, J., Schmitz, R.A., Graco, M.I., Kuypers, M.M.M., 2015. Aerobic microbial respiration in oceanic oxygen minimum zones. PLoS One 10 (7). https://doi.org/10.1371/journal.pone.0133526. (e0133526).

Khripounoff, A., Caprais, J.-C., Crassous, P., Etoubleau, J., 2006. Geochemical and biological recovery of the disturbed seafloor in polymetallic nodule fields of the Clipperton-Clarion Fracture Zone (CCFZ) at 5000-m depth. Limnol. Oceanogr. 51, 2033–2041. https://doi.org/10.4319/lo.2006.51.5.2033.

Klinkhammer, G.P., 1980. Early diagenesis in sediments from the eastern equatorial Pacific, II. Pore water metal results. Earth Planet. Sci. Lett. 49, 81–101. https://doi.org/10.1016/0012-821X(80)90151-X.

Kretschmer, S., Geibert, W., Rutgers van der Loeff, M.M., Mollenhauer, G., 2010. Grain size effects on 230Thxs inventories in opal-rich and carbonate-rich marine sediments. Earth Planet. Sci. Lett. 294, 131–142. https://doi.org/10.1016/j.epsl.2010.03.021.

Kretschmer, S., Geibert, W., Rutgers van der Loeff, M.M., Schnabel, C., Xu, S., Mollenhauer, G., 2011. Fractionation of 230Th, 231Pa, and 10Be induced by particle size and composition within an opal-rich sediment of the Atlantic Southern Ocean. Geochim. Cosmochim. Acta 75, 6971–6987. https://doi.org/10.1016/j.gca.2011.09.012.

Kuhn, T., Versteegh, G.J.M., Villinger, H., Dohrmann, I., Heller, C., Koschinsky, A., Kaul, N., Ritter, S., Wegorzewski, A.V., Kasten, S., 2017. Widespread seawater circulation in 18–22 Ma oceanic crust: impact on heat flow and sediment geochemistry. Geology 45 (9), 799–802. https://doi.org/10.1130/G39091.1.

Kuhn, G., 2013. Don't forget the salty soup: Calculations for bulk marine geochemistry and radionuclide geochronology. Goldschmidt 2013 Florence, Italy, 25 August 2013–30 August 2013. ⟨http://dx.doi.org/10.1180/minmag.2013.077.5.11⟩.

Lodge, M., Johnson, D., Le Gurun, G., Wengler, M., Weaver, P., Gunn, V., 2014. Seabed mining: international Seabed Authority environmental management plan for the Clarion–Clipperton Zone. A partnership approach. Mar. Policy 49, 66–72. https://doi.org/10.1016/j.marpol.2014.04.006.

Luther, G.W., Sundby, B., Lewis, B.L., Brendel, P.J., Silverberg, N., 1997. Interactions of manganese with the nitrogen cycle: alternative pathways to dinitrogen. Geochim. Cosmochim. Acta 61, 4043–4052. https://doi.org/10.1016/S0016-7037(97)00239-1.

Lutz, M.J., Dunbar, R.B., Caldeira, K., 2002. Regional variability in the vertical flux of particulate organic carbon in the ocean interior. Glob. Biogeochem. Cycles 16, 1037–1055.

Lutz, M.J., Caldeira, K., Dunbar, R.B., Behrenfeld, M.J., 2007. Seasonal rhythms of net primary production and particulate organic carbon flux to depth describe the efficiency of biological pump in the global ocean. J. Geophys. Res. 112, C10011. https://doi.org/10.1029/2006JC003706.

Madureira, P., Brekke, H., Cherkashov, G., Rovere, M., 2016. Exploration of polymetallic nodules in the Area: reporting practices, data management and transparency. Mar. Policy 70, 101–107. https://doi.org/10.1016/j.marpol.2016.04.051.

Martin, J.H., Knauer, G.A., Karl, D.M., Broenkow, W.W., 1987. VERTEX: carbon cycling in the northeast Pacific. Deep-Sea Res. Part A 34, 267–285.

Martínez Arbizu, P., Haeckel, M., 2015. RV SONNE Fahrtbericht/Cruise Report SO239: EcoResponse Assessing the Ecology, Connectivity and Resilience of Polymetallic Nodule Field Systems, Balboa (Panama) – Manzanillo (Mexico,) 11.03. 30.04.2015. GEOMAR Helmholtz-Zentrum für Ozeanforschung, Kiel, Germany (Report No. ⟨http://dx.doi.org/10.3289/GEOMAR_REP_NS_25_2015⟩.

Mero, J.L., 1965. The mineral resources of the Sea. Elsevier Oceanogr. Ser. 1, 312.

Mewes, K., Mogollón, J.M., Picard, A., Rühlemann, C., Kuhn, T., Nöthen, K., Kasten, S., 2014. Impact of depositional and biogeochemical processes on small scale variations in nodule abundance in the Clarion-Clipperton Fracture Zone. Deep-Sea Res. Part I: Oceanogr. Res. Pap. 91, 125–141. https://doi.org/10.1016/j.dsr.2014.06.001.

Mewes, K., Mogollón, J.M., Picard, A., Rühlemann, C., Eisenhauer, A., Kuhn, T., Ziebis, W., Kasten, S., 2016. Diffusive transfer of oxygen from seamount basaltic crust into overlying sediments: an example from the Clarion–Clipperton Fracture Zone. Earth Planet. Sci. Lett. 433, 215–225. https://doi.org/10.1016/j.epsl.2015.10.028.

Miljutin, D.M., Miljutina, M.A., Martínez Arbizu, P., Galeron, J., 2011. Deep-sea nematode assemblage has not recovered 26 years after experimental mining of polymetallic nodules (CCFZ, Pacific). Deep-Sea Res. Part I: Oceanogr. Res. Pap. 58, 885–897.

Mogollón, J.M., Mewes, K., Kasten, S., 2016. Quantifying manganese and nitrogen cycle coupling in manganese-rich, organic carbon-starved marine sediments: examples from the Clarion-Clipperton fracture zone. Geophys. Res. Lett. 43https://doi.org/10.1002/2016GL069117. (2016GL069117).

Mohn, C., Beckmann, A., 2002. The upper ocean circulation at Great Meteor Seamount. Ocean Dyn. 52, 179–193. https://doi.org/10.1007/s10236-002-0017-4.

Müller, P.J., 1977. CN ratios in Pacific deep-sea sediments: effect of inorganic ammonium and organic nitrogen compounds sorbed by clays. Geochim. Cosmochim. Acta 41, 765–776. https://doi.org/10.1016/0016-7037(77)90047-3.

Müller, P.J., Mangini, A., 1980. Organic carbon decomposition rates in sediments of the pacific manganese nodule belt dated by 230Th and 231Pa. Earth Planet. Sci. Lett. 51, 94–114. https://doi.org/10.1016/0012-821X(80)90259-9.

Müller, P.J., Suess, E., 1979. Productivity, sedimentation rate, and sedimentary organic matter in the oceans—I. Organic carbon preservation. Deep-Sea Res. Part A Oceanogr. Res. Pap. 26, 1347–1362. https://doi.org/10.1016/0198-0149(79)90003-7.

Müller, P.J., Hartmann, M., Suess, E., 1988. The chemical environment of pelagic sediments. In: Halbach, P., Friedrich, G., von Stackelberg, U. (Eds.), The Manganese Nodule Belt of the Pacific Ocean: Geological Environment, Nodule Formation, and Mining Aspects. Enke, Stuttgart, pp. 70–90.

Murray, J., Renard, A.F., 1891. Deep-sea Deposits (Based on the Specimens Collected during the Voyage of HMS Challenger in the Years 1872 to 1876). Report on the Scientific Results of the Voyage of H.M.S. Challenger during the Years. John Menzies and Co., Edinburgh, United Kingdom, pp. 1873–1876.

Murray, J.W., Grundmanis, V., 1980. Oxygen consumption in pelagic marine sediments. Science 209, 1527–1530. https://doi.org/10.1126/science.209.4464.1527.

Murray, J.W., Kuivila, K.M., 1990. Organic matter diagenesis in the northeast Pacific: transition from aerobic red clay to suboxic hemipelagic sediments. Deep-Sea Res. Part A. Oceanogr. Res. Pap. 37, 59–80. https://doi.org/10.1016/0198-0149(90)90029-U.

Nöthen, K., Kasten, S., 2011. Reconstructing changes in seep activity by means of pore water and solid phase Sr/Ca and Mg/Ca ratios in pockmark sediments of the Northern Congo Fan. Mar. Geol. 287, 1–13. https://doi.org/10.1016/j.margeo.2011.06.008.

Park, C.B., Clark, D.S., 2002. Rupture of the Cell Envelope by Decompression of the Deep-Sea Methanogen Methanococcus jannaschii. Appl. Environ. Microbiol. 68, 1458–1463.

Redfield, A.C., 1934. On the proportions of organic derivations in sea water and their relation to the composition of plankton. In: Daniel, R.J. (Ed.), James Johnstone Memorial Volume. University Press of Liverpool, pp. 176–192.

Revsbech, N.P., 1989. An oxygen microsensor with a guard cathode. Limnol. Oceanogr. 34, 474–478. https://doi.org/10.4319/lo.1989.34.2.0474.

Røy, H., Kallmeyer, J., Adhikari, R.R., Pockalny, R., Jørgensen, B.B., D'Hondt, S., 2012. Aerobic microbial respiration in 86-Million-Year-Old Deep-Sea Red Clay. Science 336, 922–925. https://doi.org/10.1126/science.1219424.

Rühlemann, C., Kuhn, T., Wiedicke, M., Kasten, S., Mewes, K., Picard, A., 2011. Current status of manganese nodule exploration in the German license area. In: Proceedings of the 9th ISOPE Ocean Mining Symposium. International Society of Offshore and Polar Engineers, Maui, Hawaii, pp. 168–173.

Seeberg-Elverfeldt, J., Schlüter, M., Feseker, T., Kölling, M., 2005. Rhizon sampling of porewaters near the sediment-water interface of aquatic systems. Limnol. Oceanogr. Methods 3, 361–371. https://doi.org/10.4319/lom.2005.3.361.

Smith, C.R., De Leo, F.C., Bernardino, A.F., Sweetman, A.K., Arbizu, P.M., 2008. Abyssal food limitation, ecosystem structure and climate change. Trends Ecol. Evol. 23 (9), 518–528.

Soetaert, K., Meysman, F., 2012. Reactive transport in aquatic ecosystems: Rapid model prototyping in the open source software R. Environ. Model. Softw. 32, 49–60. https://doi.org/10.1016/j.envsoft.2011.08.011.

Soetaert, K., Petzoldt, T., Setzer, R.W., 2010. Solving differential equations in R: package deSolve. J. Stat. Softw. 33 (9), 1–25.

von Stackelberg, U., Beiersdorf, H., 1987. Manganese nodules and sediments in the equatorial North Pacific Ocean. Geol. Jahrb. D 87.

von Stackelberg, U., Beiersdorf, H., 1991. The formation of manganese nodules between the Clarion and Clipperton fracture zones southeast of Hawaii. Mar. Geol. Geol. Geophys. Mineral. Resour. S. Pac. 98, 411–423. https://doi.org/10.1016/0025-3227(91)90113-I.

Stanley, D.J., Taylor, P.T., 1977. Sediment transport down a seamount flank by a combined current and gravity process. Mar. Geol. 23, 77–88.

Suess, E., 1980. Particulate organic carbon flux in the oceans—surface productivity and oxygen utilization. Nature 288, 260–263. https://doi.org/10.1038/288260a0.

Theyer, F., Mayer, L.A., Scotia, N., Barron, J.A., 1985. 33. the Equatorial Pacific High-productivity Bell Elements for A Synthesis of Deep Sea Drilling Project Leg 85 Results1.

Turnewitsch, R., Reyss, J.-L., Chapman, D.C., Thomson, J., Lampitt, R.S., 2004. Evidence for a sedimentary fingerprint of an asymmetric flow field surrounding a short seamount. Earth Planet. Sci. Lett. 222, 1023–1036. https://doi.org/10.1016/j.epsl.2004.03.042.

Turnewitsch, R., Lahajnar, N., Haeckel, M., Christiansen, B., 2015. An abyssal hill fractionates organic and inorganic matter in deep-sea surface sediments. Geophys. Res. Lett. 42, 7663–7672. https://doi.org/10.1002/2015GL065658.

Tyrell, T., 1999. The relative influences of nitrogen and phosphorus on oceanic primary production. Nature 400, 525–531.

Vanreusel, A., Hilario, A., Ribeiro, P.A., Menot, L., Arbizu, P.M., 2016. Threatened by mining, polymetallic nodules are required to preserve abyssal epifauna. Sci. Rep. 6, 26808. https://doi.org/10.1038/srep26808.

Wegorzewski, A.V., Kuhn, T., 2014. The influence of suboxic diagenesis on the formation of manganese nodules in the Clarion Clipperton nodule belt of the Pacific Ocean. Mar. Geol. 357, 123–138. https://doi.org/10.1016/j.margeo.2014.07.004.

Wessel, P., Smith, W.H.F., Scharroo, R., Luis, J., Wobbe, F., 2013. Generic Mapping Tools: Improved Version Released. EOS Trans 94. AGU, pp. 409–410. https://doi.org/10.1002/2013EO450001.

Whittaker, J., Goncharov, A., Williams, S., Müller, R.D., Leitchenkoy, G., 2013. Global sediment thickness dataset updated for the Australian-Antarctic Southern Ocean. Geochem. Geophys. Geosystems. https://doi.org/10.1002/ggge.20181.

Wishner, K.F., Ashjian, C.J., Gelfman, C., Gowing, M.M., Kann, L., Levin, L.A., Mullineaux, L.S., Saltzman, J., 1995. Pelagic and benthic ecology of the lower interface of the Eastern Tropical Pacific oxygen minimum zone. Deep-Sea Res. Part I: Oceanogr. Res. Pap. 42, 93–115. https://doi.org/10.1016/0967-0637(94)00021-J.

Xu, G., Lavelle, J.W., 2017. Circulation, hydrography, and transport over the summit of Axial Seamount, a deep volcano in the Northeast Pacific. J. Geophys. Res. Oceans 122, 5404–5422. https://doi.org/10.1002/2016JC012464.

Ziebis, W., McManus, J., Ferdelman, T., Schmidt-Schierhorn, F., Bach, W., Muratli, J., Edwards, K.J., Villinger, H., 2012. Interstitial fluid chemistry of sediments underlying the North Atlantic gyre and the influence of subsurface fluid flow. Earth Planet. Sci. Lett. 323–324, 79–91. https://doi.org/10.1016/j.epsl.2012.01.018.

Zonneveld, K.A.F., Versteegh, G.J.M., Kasten, S., Eglinton, T.I., Emeis, K.C., Huguet, C., Koch, B.P., de Lange, G.J., Middelburg, J.J., Mollenhauer, G., Prahl, F.G., Rethemeyer, J., Wakeham, S.G., 2010. Selective preservation of organic matter in marine environments; processes and impact on the sedimentary records. Biogeosciences 7, 483–511.